geosciences

MDPI

Article

Sedimentary Fabric and Diagenetic-Fluid Controls on Pore-Structure Heterogeneity in the Deep Cretaceous Yageliemu Formation, Kuqa Depression, Tarim Basin, NW China

Lu Zhou [1], Xinyu Sun [1], Minggang Tang [1], Hong Lou [1], Jian Wang [2,3,*], Zhenhan Zhang [2,3], Jinfeng Feng [1] and Haihua Qiu [1]

[1] Tarim Oilfield Company, PetroChina, Korla 841000, China; zhoulu-tlm@petrochina.com.cn (L.Z.); s1s23010019@163.com (X.S.); tangmg-tlm@petrochina.com.cn (M.T.); louh-tlm@petrochina.com.cn (H.L.); fengjf-tlm@petrochina.com.cn (J.F.); qiuhh-tlm@petrochina.com.cn (H.Q.)
[2] State Key Laboratory of Deep Oil and Gas, Qingdao 266580, China; s24010031@s.upc.edu.cn
[3] School of Geosciences, China University of Petroleum (East China), Qingdao 266580, China
* Correspondence: wangjian8601@upc.edu.cn

Abstract

Deep Cretaceous clastic reservoirs in the Kuqa Depression are major targets for natural gas exploration in the Tarim Basin. Recent exploration of the Yageliemu Formation in the Ketan area has revealed considerable resource potential, although reservoir performance is strongly affected by deep burial, compaction, repeated fluid–rock interaction, and pronounced pore-system heterogeneity. Core descriptions, epoxy-impregnated thin sections, cathodoluminescence, scanning electron microscopy, conventional petrophysical measurements, mercury intrusion capillary pressure, and nuclear magnetic resonance data were integrated to evaluate sedimentary fabric, reservoir-space types, pore-throat characteristics, and diagenetic modification. The succession was deposited mainly in a braided river delta plain setting and is dominated by medium sandstone, pebbly sandstone, and fine conglomerate. Overall reservoir quality is poor, with an average porosity of 3.4% and permeability commonly between 0.01 and 0.5 mD. MICP and NMR data distinguish four pore-structure types. From Type I to Type IV, average displacement pressure rises from 0.89 to 11.02 MPa, whereas median throat radius and movable-fluid porosity decline from 0.17 to 0.01 μm and from 2.00% to 0.72%, respectively. Residual intergranular pores constitute the main storage space, while feldspar- and lithic-fragment-dissolution pores provide additional local storage. Fractures contribute little pore volume but can markedly improve connectivity where they remain open or only weakly cemented. The present reservoir heterogeneity reflects the combined effects of sand-body stacking, sandstone–mudstone arrangement, fault-related fracturing, and multistage diagenesis. The most favorable intervals occur in thick, relatively clean stacked sand bodies where residual pores are preserved, dissolution pores remain connected to the throat network, and fractures have undergone limited late-stage filling.

Keywords: Yageliemu Formation; sedimentary fabric; pore-throat heterogeneity; diagenetic fluids; deep clastic reservoir

Check for updates

Academic Editor: Eun Young Lee

Received: 7 July 2026
Revised: 12 August 2026
Accepted: 17 August 2026
Published: 20 August 2026

Copyright: © 2026 by the authors. Licensee MDPI, Basel, Switzerland. This article is an open access article distributed under the terms and conditions of the Creative Commons Attribution (CC BY) license.

1. Introduction

The Kuqa Depression, located along the northern margin of the Tarim Basin, is one of the most important foreland basins for deep to ultra-deep natural gas exploration in China. In the broader Tarim Basin, hydrocarbon exploration has progressively extended from deep to ultra-deep and even 10,000 m scale targets, highlighting the strategic significance of deep reservoir research [1]. With continued exploration and development of major producing intervals such as the Bashijiqike Formation, new Cretaceous targets have become increasingly important for reserve growth and production replacement in deep natural gas systems [2–4]. In particular, recent exploration success in the Yageliemu Formation of the Ketan area has demonstrated promising natural gas potential [3]. However, compared with the relatively well-studied Bashijiqike Formation, the Yageliemu Formation differs markedly in sedimentary system, detrital composition, reservoir space types, and diagenetic modification. Its effective reservoir development conditions and pore structure evolution remain poorly understood.

For deep clastic reservoirs, reservoir quality cannot be adequately evaluated by porosity or permeability alone. The storage and flow capacity of such reservoirs are controlled more fundamentally by pore-throat configuration, fracture connectivity, and the spatiotemporal coupling of diagenetic processes [5–9]. Previous studies have shown that effective reservoirs in deep tight sandstones of the Kuqa Depression are controlled jointly by sedimentation and diagenesis: initial sedimentary fabric determines grain-support style, grain-size differentiation, and sandstone–mudstone architecture, whereas subsequent compaction, cementation, dissolution, and fracturing continuously reshape the microscopic pore system and seepage capacity [2,4,6–9]. Therefore, an integrated analysis of sedimentary fabric, reservoir space types, pore-throat characteristics, and diagenetic evolution is essential for revealing the development mechanism of effective reservoirs in the Yageliemu Formation. Comparable studies from other sandstone reservoirs likewise show that depositional facies, grain size, sorting, and sand-body architecture establish the initial reservoir framework, whereas compaction, cementation, dissolution, and authigenic clay precipitation subsequently accentuate reservoir heterogeneity [10–12].

Existing studies of deep Cretaceous clastic reservoirs in the Kuqa Depression have focused predominantly on the Bashijiqike Formation, whereas investigations of the Yageliemu Formation have mainly addressed regional tectonic setting, sedimentary facies distribution, and basic reservoir properties [3,13,14]. Consequently, several important issues remain unresolved. First, quantitative variations in pore-throat structure among different grain-size intervals and sandstone–mudstone architectural units have not been systematically characterized. Second, the relative contributions of compaction, carbonate cementation, dissolution, and fracture-related fluid migration to pore preservation and connectivity remain poorly constrained. Third, the sedimentary–diagenetic combinations favorable for preserving connected intergranular pores, dissolution pores, and fractures have not been clearly identified. These uncertainties limit the evaluation of reservoir effectiveness and the prediction of favorable intervals in the Yageliemu Formation.

Accordingly, this study addresses three specific research questions. First, does sedimentary architecture primarily establish the initial framework of pore–system heterogeneity, whereas subsequent diagenesis determines the preservation and connectivity of that framework? Second, which reservoir space components—residual intergranular pores, dissolution pores, or fractures—make the greatest contribution to effective storage and fluid flow in the deeply buried Yageliemu Formation? Third, how do different sedimentary architectural elements, including thick stacked sand bodies, sandstone–mudstone interbeds, and the marginal parts of individual sand bodies, differ in pore-throat structure and fluid mobility? To address these questions, core observations, petrographic

and cathodoluminescence analyses, scanning electron microscopy, petrophysical measurements, mercury intrusion capillary pressure, nuclear magnetic resonance, carbonate geochemistry, and fluid-inclusion data were integrated. This approach allows the respective roles of sedimentary preconditioning, diagenetic modification, and fracture-related fluid migration in controlling reservoir heterogeneity to be evaluated.

2. Geological Setting

The Tarim Basin in northwestern China is a large superimposed basin developed on a Precambrian cratonic basement (Figure 1a). Its Phanerozoic evolution was strongly influenced by the surrounding orogenic belts and was characterized by long-term basin–mountain coupling [15,16]. The Kuqa Depression is located along the northern margin of the Tarim Basin at the southern foot of the Tianshan Mountains (Figure 1b). It represents a typical foreland basin unit between the Tarim Basin and the South Tianshan orogenic belt and has been strongly modified by late Cenozoic compression, forming a prominent fold-and-thrust structural system [17–20]. The Kelasu structural belt, situated in the northwestern Kuqa Depression (Figure 1c), is one of the most intensely deformed and gas rich structural units in the region and is characterized by ultra-deep fractured tight sandstone reservoirs and pronounced reservoir heterogeneity [17–22]. The Ketan area and the principal wells involved in this study are shown in Figure 1d.

Tectonically, the Kuqa Depression has evolved since the Late Cretaceous from a stage of weak tectonic activity to rapid shortening under strong compression. During the latest Oligocene to early Miocene, fold-and-thrust structures began to develop. Since the late Miocene, foreland propagating thrusting intensified, shortening accelerated markedly, and the present day complex structural pattern of the Kelasu structural belt was progressively established [17–19]. Strong compressional deformation shaped the deep trap systems and also modified the pore–fracture network through fault activity, fracture development, and fluid migration [4,7].

The Cretaceous succession of the Kuqa Depression is dominated by the Lower Cretaceous, which generally comprises, from bottom to top, the Yageliemu, Shushanhe, Baxigai, and Bashijiqike formations. The Yageliemu Formation is an important deep reservoir interval in the study area and is relatively stable in thickness. It is overlain by thick mudstones of the Shushanhe Formation, which provided favorable conditions for sandstone–mudstone architectural differentiation and subsequent fluid–rock interaction [3,5,13,14,23]. Regionally, the Yageliemu Formation was deposited mainly in alluvial fan, fan delta, and braided river delta systems. In the Ketan area, it is dominated by braided river delta plain deposits consisting mainly of pebbly sandstone and fine conglomerate [3,13,14,23].

A generalized chronostratigraphic and lithostratigraphic column of the Kuqa Depression was compiled to show the principal stratigraphic units, lithologies, depositional environments, source–reservoir–cap rock assemblages, detachment layers, and tectonic stages (Figure 2). The Lower Cretaceous Yageliemu Formation is highlighted as the target interval of this study. In the Ketan area, it is dominated by braided river delta plain deposits composed mainly of pebbly sandstone, medium sandstone, and fine conglomerate.

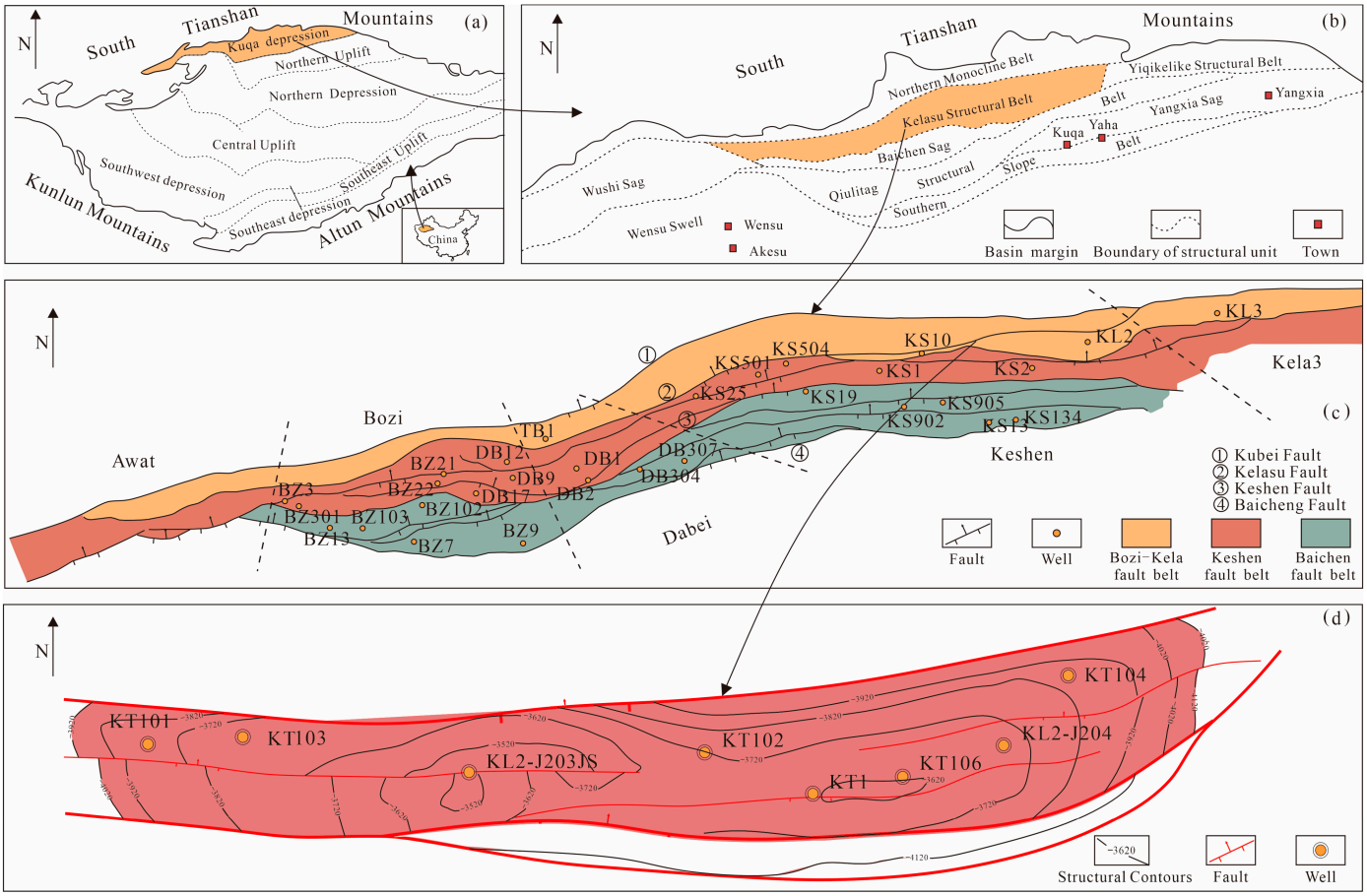


Figure 1. Geological location and structural framework of the study area. (**a**) Structural map of the Tarim Basin, with an inset showing its location within China; (**b**) structural map of the Kuqa Depression; (**c**) structural framework of the Kelasu structural belt, showing the four major faults (① Kubei Fault, ② Kelasu Fault, ③ Keshen Fault, and ④ Baicheng Fault). The four dashed lines divide the belt into five structural blocks, namely Awat, Bozi, Dabei, Keshen, and Kela 3; (**d**) structural map of the Ketan area, showing the locations of the investigated wells, faults, and structural contours.

The Ketan area provides a suitable natural laboratory for evaluating the coupled controls of sedimentary architecture and diagenesis on pore system evolution for three reasons. First, repeated channel migration and vertical sand-body stacking within the braided river delta plain generated marked variations in grain size, sorting, sand-body thickness, and sandstone–mudstone configuration, allowing the influence of depositional architecture on the initial pore framework to be assessed [3,13,14,23]. Second, the Yageliemu Formation has experienced deep burial and multistage diagenetic modification, including compaction, carbonate and siliceous cementation, dissolution, and clay-mineral transformation, providing an opportunity to evaluate how the initial sedimentary framework was preserved or overprinted during burial. Third, strong compressional deformation in the Kelasu structural belt produced fractures that acted both as potential flow pathways and as sites of later mineral precipitation [4,7,17–20]. Therefore, the coexistence of contrasting sedimentary architectures, multistage diagenetic products, and variably filled fractures makes the Ketan area particularly suitable for distinguishing sedimentary preconditioning from subsequent diagenetic and fracture-related modification of pore structure.

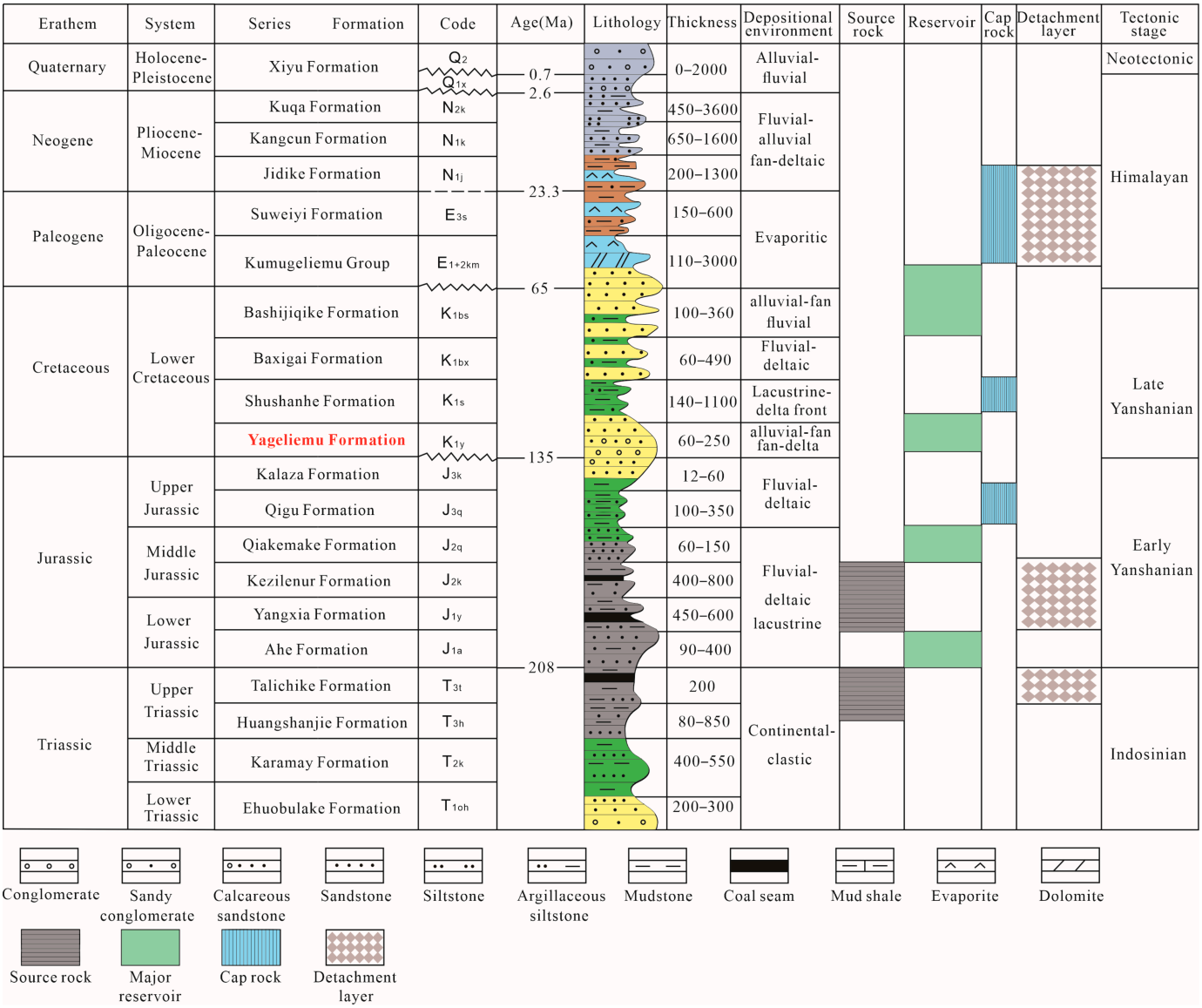


Figure 2. Generalized chronostratigraphic and lithostratigraphic column of the Kuqa Depression, showing the principal stratigraphic units, lithologies, depositional environments, source–reservoir–cap rock assemblages, detachment layers, and tectonic stages. Colors in the lithological column indicate the observed rock colors, whereas lithologies are distinguished by the patterns shown in the legend. Darker rock colors were slightly lightened to improve visual clarity and facilitate identification of the lithological patterns. Modified after Zeng et al. [24].

3. Materials and Methods

3.1. Sampling and Core Description

Core samples were obtained from the Lower Cretaceous Yageliemu Formation in six wells—KL2-J203JS, KL2-J204, KT1, KT102, KT104, and KT106—located in the Ketan area (Figure 1d). The sampled intervals range from approximately 5100 to 5600 m. A total of 159 samples were systematically collected at broadly even intervals from sandstone and mudstone sections to represent the principal lithologies and sandstone–mudstone configurations of the study interval. Core observations documented lithology, sedimentary structures, sand-body contacts, fracture development, and visible cementation.

3.2. Petrographic, Cathodoluminescence, and Scanning Electron Microscopy (SEM) Analyses

A total of 144 epoxy-impregnated thin sections were prepared for petrographic analysis. Blue-dyed epoxy resin was used to enhance pore visibility, and carbonate staining was applied to assist in identifying carbonate minerals. Petrographic observations were conducted using a Zeiss Axioscope 5 polarizing microscope (Carl Zeiss Microscopy GmbH, Jena, Germany) in accordance with SY/T 5368-2016, Identification for Thin Section of Rocks [25]. Detrital composition and textural characteristics were identified and semi-quantitatively estimated under plane- and cross-polarized light. The observations included lithology, the relative contents of quartz, feldspar, and lithic fragments, grain size, sorting, roundness, grain-contact relationships, matrix and cement contents, pore types, fractures, authigenic minerals, and diagenetic textures. For ternary classification, the Q–F–R components and the principal lithic fragment groups were separately recalculated to 100% before plotting.

Based on the petrographic observations, 64 representative samples containing carbonate cements were selected for cathodoluminescence analysis. Polished thick sections were examined using a Cambridge CL8200 MK5 cathodoluminescence detector (Cambridge Image Technology Ltd., Hatfield, UK) mounted on the Zeiss microscope to distinguish different generations and occurrences of carbonate cements, consistent with established cathodoluminescence applications in sandstone diagenetic studies [26,27]. Cathodoluminescence images were acquired at an accelerating voltage of 10 kV and a beam current of 250 μA. Exposure times were 10 s, 30 s, and 60 s at magnifications of 50×, 100×, and 200×, respectively.

SEM analysis was conducted on 16 polished samples using a Zeiss Crossbeam 550 scanning electron microscope (Carl Zeiss Microscopy GmbH, Jena, Germany). The samples were gold coated before analysis. Backscattered-electron imaging was used to characterize authigenic minerals, dissolution textures, mineral–pore relationships, and micropore occurrence, and energy-dispersive X-ray spectroscopy was used to identify mineral phases. The operating conditions were adjusted according to the observed features; one representative image was acquired at an accelerating voltage of 25 kV, a magnification of 1000×, and a working distance of 10.4 mm.

3.3. Petrophysical and Pore-Structure Analyses

Conventional porosity and gas permeability measurements were conducted on cylindrical core-plug samples in accordance with GB/T 29172-2012, Practices for Core Analysis [28]. A total of 72 samples were submitted, and 69 valid conventional petrophysical results were retained. Porosity was measured using an UltraPore-300 helium porosimeter (Core Laboratories, Houston, TX, USA) under laboratory ambient conditions of 24.0 °C and 90.70 kPa. Gas permeability was measured using a K-2 gas permeameter (Research Institute of Tarim Oilfield Company, PetroChina, Korla, China), with gas flow monitored using a 10 mL soap film flowmeter, under laboratory ambient conditions of 25.0 °C and 90.20 kPa. Sample dimensions were measured using a digital caliper with a measuring range of 0–150 mm.

High-pressure mercury intrusion capillary pressure (MICP) measurements were performed on 56 samples using an AutoPore IV 9500 mercury porosimeter (Micromeritics Instrument Corporation, Norcross, GA, USA) in accordance with GB/T 29171-2023 [29]. Pore-throat radii were interpreted from capillary pressure using the Washburn relation [30]. The measurements were conducted at 25.0 °C and an ambient pressure of 100.8 kPa. The MICP dataset comprised 16 Type I, 23 Type II, 10 Type III, and 7 Type IV samples. Displacement pressure, median capillary pressure, median throat radius, mean pore-throat radius, mer-

cury withdrawal efficiency, sorting coefficient, and homogeneity coefficient were obtained from the intrusion–extrusion data.

Low-field nuclear magnetic resonance (NMR) measurements were performed on 47 water-saturated samples using a MicroMR02-11n NMR analyzer (Suzhou Niumag Analytical Instrument Co., Ltd., Suzhou, China) in accordance with SY/T 6490-2023 [31]. The laboratory ambient conditions were 24.5 °C and 100.9 kPa, whereas the measurement temperature was maintained at 32 °C using a 1-inch probe. The acquisition parameters were as follows: resonance frequency, 12 MHz; echo spacing, 0.2 ms; acquisition delay, 0.05 ms; sampling frequency, 200 kHz; waiting time, 5000 ms; number of echoes, 2048; number of scans, 512; accumulation number, 32; digital gain, 3; and analog gain, 20.0 dB. The NMR dataset comprised 8 Type I, 10 Type II, 15 Type III, and 14 Type IV samples. The T_2 cutoff, bound-fluid porosity and saturation, and movable-fluid porosity and saturation were determined by comparing the water-saturated and post-centrifugation T_2 distributions, following the established centrifugation-based NMR approach for tight sandstones [32].

The four pore-structure types were defined by integrating MICP curve morphology, displacement and median capillary pressures, throat-radius distributions, water-saturated T_2 spectral shapes, and bound- and movable-fluid parameters. Samples displaying internally consistent combinations of these characteristics were assigned to the same type; no single parameter was used as the sole classification criterion.

3.4. Fluid-Inclusion Microthermometry

Fluid-inclusion microthermometry was conducted using a THMSG600 heating–freezing stage (Linkam Scientific Instruments Ltd., Salfords, Surrey, UK) mounted on a Zeiss Axioscope 5 microscope in accordance with EJ/T 1105-1999, Determination of Temperature of Fluid Inclusions in Minerals [33]. Petrographic selection and interpretation of fluid inclusions followed established principles for sedimentary and diagenetic systems [34]. Representative fluid inclusions hosted in quartz overgrowths and pore-filling authigenic quartz were selected based on their petrographic occurrence, and homogenization temperatures were measured to constrain the temperature conditions of diagenetic-fluid activity.

The petrographic, petrophysical, MICP, NMR, geochemical, and fluid-inclusion datasets were compared by sample depth, lithology, sedimentary architecture, and pore-structure type to evaluate the relationships among sedimentary fabric, pore types, diagenetic minerals, pore-throat characteristics, and fluid mobility.

4. Results

4.1. Sedimentary Structures and Petrographic Characteristics

Core observations of the Yageliemu Formation reveal medium- to large-scale cross-bedding with clearly inclined laminae (Figure 3a), sharp contacts and local erosional truncation between siltstone and mudstone (Figure 3b), and calcite-filled high-angle fractures cutting cross-bedded sandstone (Figure 3c). Abrupt grain-size changes occur between sandstone and pebbly sandstone (Figure 3d,e), whereas an erosional scour surface separates conglomerate from fine sandstone (Figure 3f). Locally oriented pebble long axes (Figure 3g), mud clasts within sandy conglomerate (Figure 3h), and well-developed high-angle cross-bedding (Figure 3i) are also common.

Petrographically, the Yageliemu Formation reservoirs are composed mainly of medium sandstone, pebbly sandstone, and fine conglomerate. Grain-size distributions vary among the investigated wells (Figure 4a). Most samples are moderately sorted (Figure 4b), and the detrital grains are predominantly subangular to subrounded (Figure 4c).

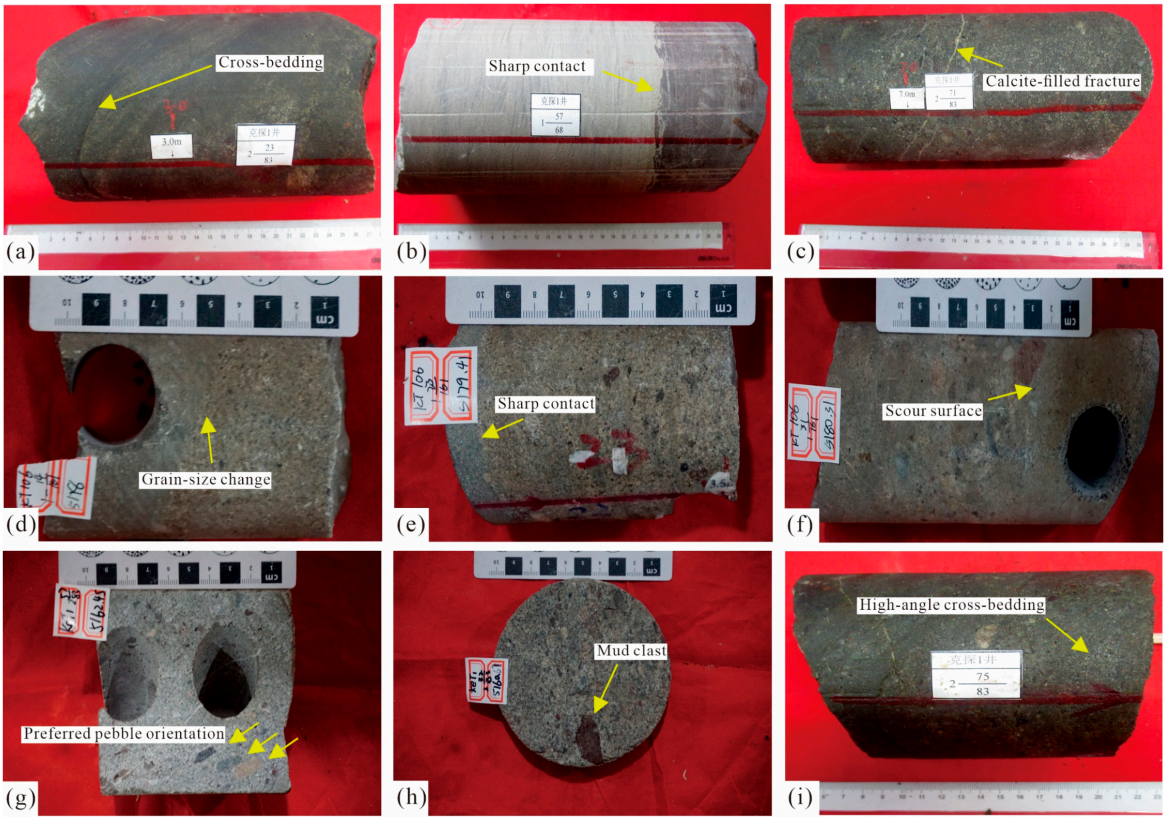


Figure 3. Typical sedimentary structures in core samples from the Cretaceous Yageliemu Formation in the Ketan area, Kuqa Depression. (**a**) Medium- to large-scale cross-bedding in sandstone, KT1, 5159.5 m; (**b**) sharp contact and local erosional truncation between siltstone and mudstone, KT1, 5056.15 m; (**c**) calcite-filled high-angle fractures cutting cross-bedded sandstone, KT1, 5163.5 m; (**d**) abrupt grain-size change between grey sandstone and pebbly sandstone, KT106, 5178 m; (**e**) poorly sorted pebbly sandstone in sharp contact with underlying finer-grained sandstone, KT106, 5179.41 m; (**f**) erosional scour surface between conglomerate and fine sandstone, KT106, 5178 m; (**g**) preferential orientation of pebble long axes in conglomerate, KT1, 5162.45 m; (**h**) mud clasts within sandy conglomerate, KT1, 5160.67 m; (**i**) high-angle cross-bedding, KT1, 5163.95 m. The Chinese text "克探1井" visible on the original core labels denotes Well KT1; other handwritten markings are original sample identifiers.

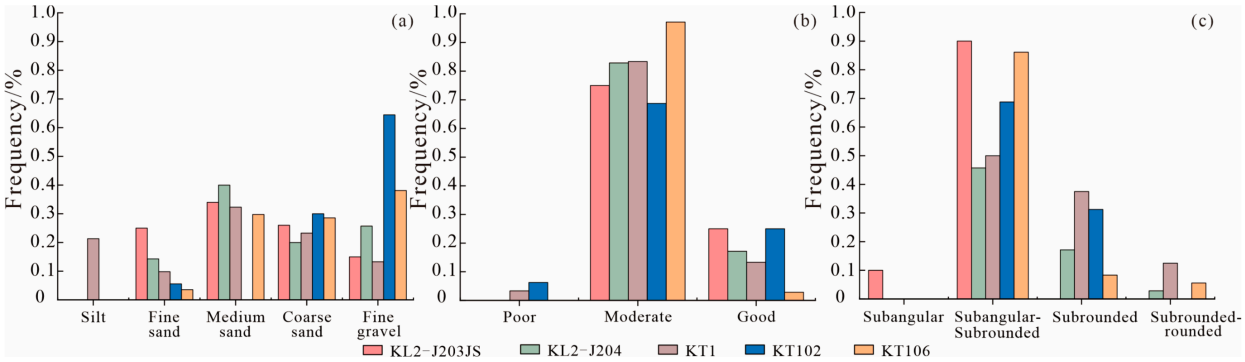


Figure 4. Grain-size, sorting, and roundness characteristics of clastic reservoir rocks in the Yageliemu Formation. (**a**) Frequency histogram of clastic grain-size distribution; (**b**) frequency histogram of sorting degree; (**c**) frequency histogram of roundness.

The Q–F–R compositions indicate that the major sandstone types include litharenite, feldspathic litharenite, feldspar-bearing litharenite, and lithic arkose (Figure 5). Lithic frag-

ments are dominated by metamorphic and igneous rock fragments, whereas sedimentary lithic fragments are less abundant (Figure 6).

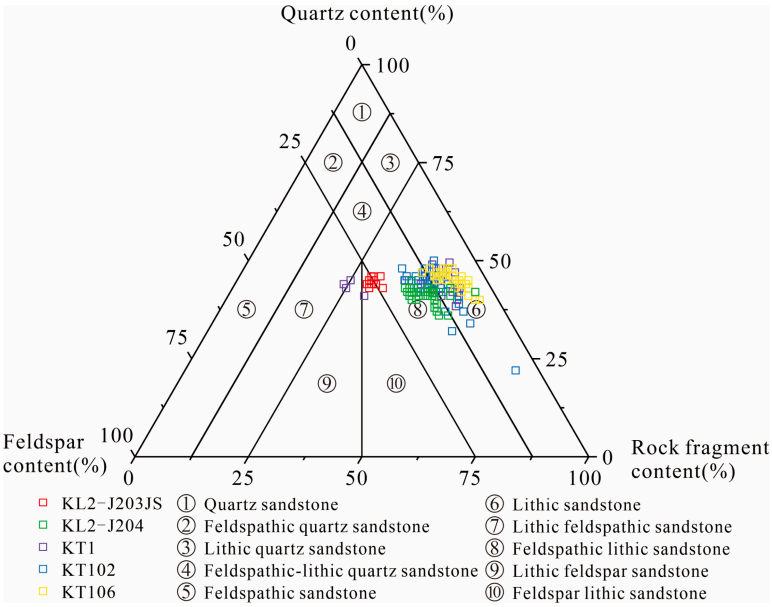


Figure 5. Q–F–R ternary diagram showing sandstone classifications of samples from the Yageliemu Formation.

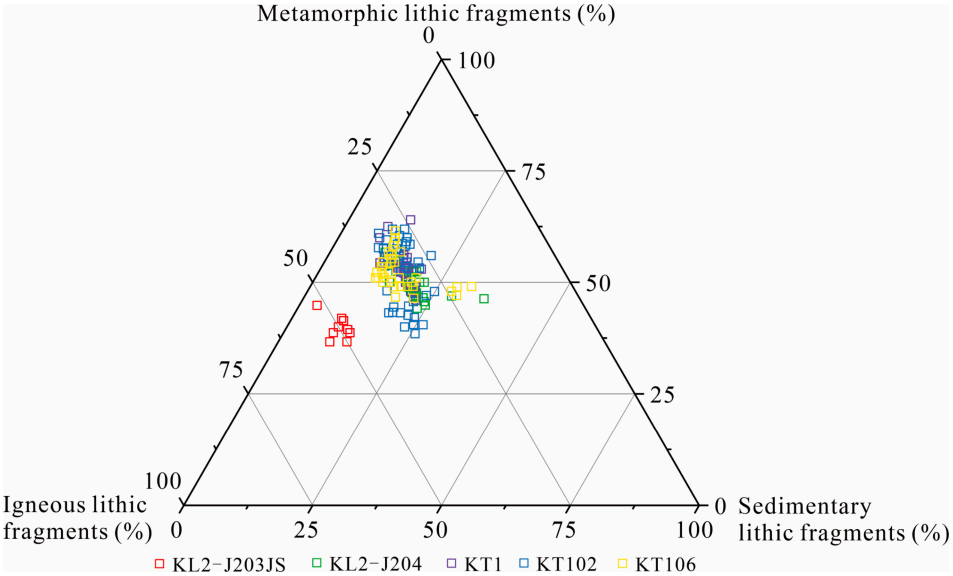


Figure 6. Lv–Lm–Ls ternary diagram showing lithic fragment compositions of the Yageliemu Formation samples.

4.2. Reservoir Space Types and Petrophysical Properties

Petrophysical measurements show that porosity is mainly between 2% and 8%, with an average of 3.4%, whereas permeability is mainly between 0.01 and 0.5 mD (Figure 7). The porosity–permeability data are widely scattered and show no clear linear relationship.

Microscopic observations show that residual primary intergranular pores commonly occur as irregular wedge-shaped or triangular spaces among detrital grains (Figure 8a–d,f). Feldspar dissolution pores are locally developed within unstable grains (Figure 8e). Other secondary pores include lithic-fragment dissolution pores and local moldic pores. Partially filled late-stage fractures are present in some samples (Figure 8g), whereas microfracture assemblages locally cut grains and connect adjacent pore domains (Figure 8h,i).

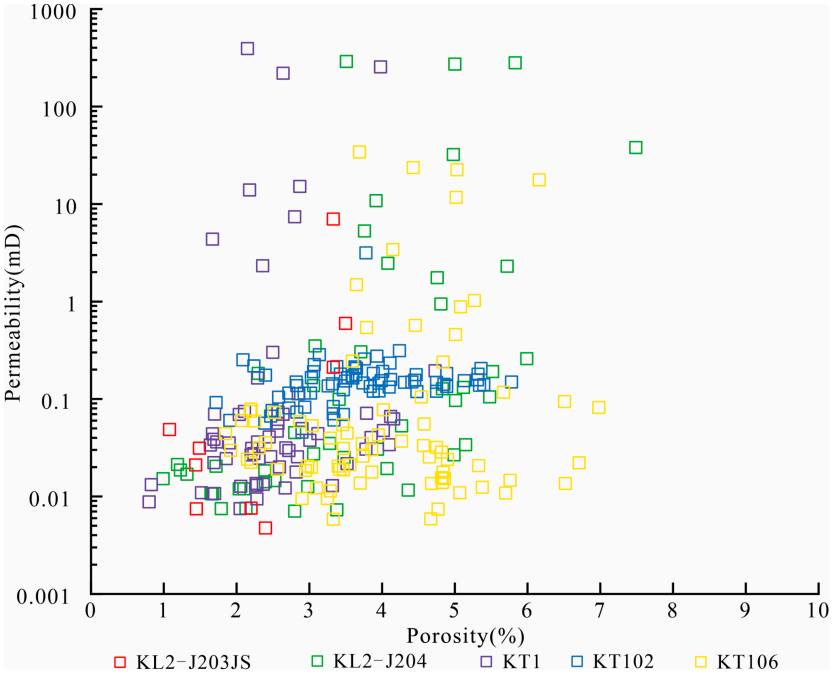


Figure 7. Porosity–permeability cross plot of the Yageliemu Formation sandstones.

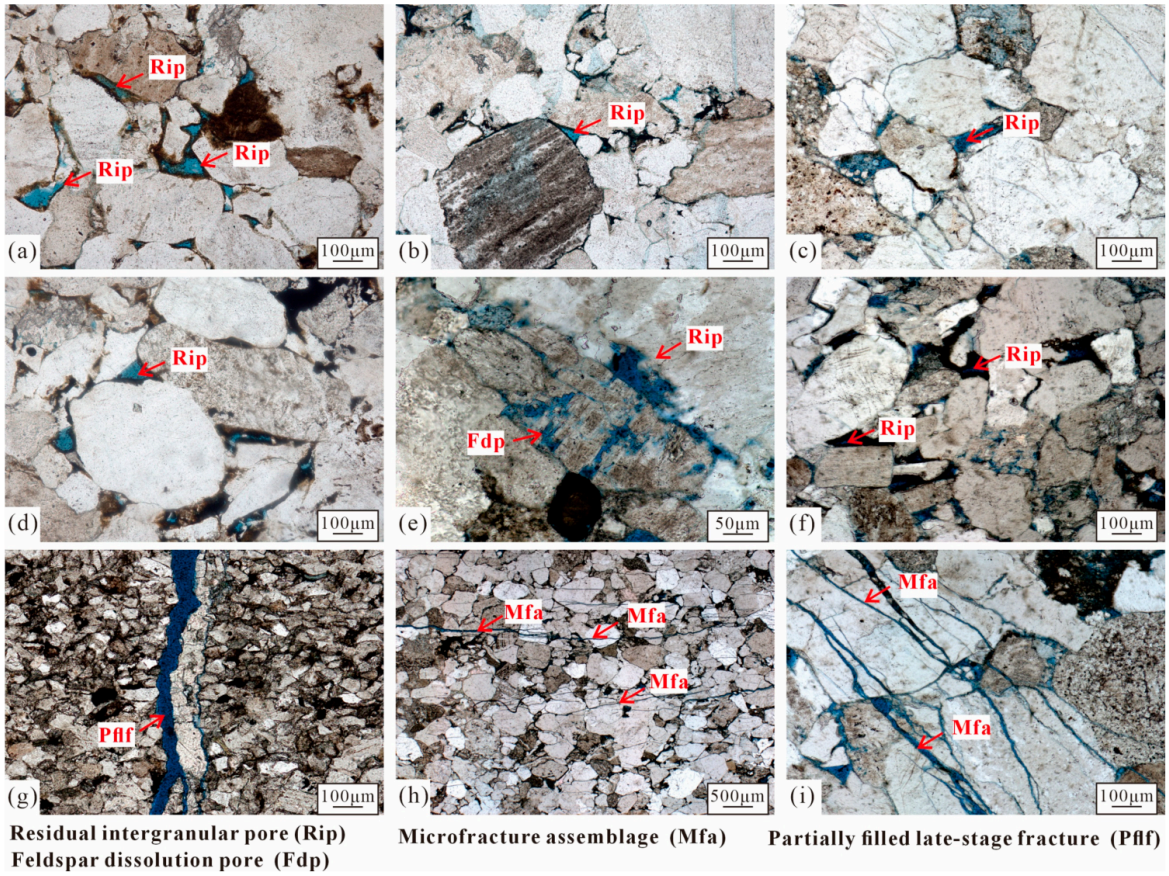


Figure 8. Typical reservoir space types in the Yageliemu Formation sandstones. (**a**) Residual primary intergranular pore; (**b**) residual primary intergranular pore; (**c**) residual primary intergranular pore; (**d**) residual primary intergranular pore; (**e**) feldspar dissolution pore; (**f**) residual primary intergranular pore; (**g**) partially filled late-stage fracture; (**h**) microfracture assemblage; (**i**) microfracture assemblage. Abbreviations: Rip, residual intergranular pore; Fdp, feldspar dissolution pore; Mfa, microfracture assemblage; Pflf, partially filled late-stage fracture.

4.3. Pore-Throat Structure Characteristics and Heterogeneity

Integrated MICP (n = 56) and NMR (n = 47) results allow the pore systems of the Yageliemu Formation to be divided into four types. The classification combines intrusion–extrusion curve morphology, characteristic capillary-pressure and throat-radius parameters, water-saturated T_2 spectral distributions, and bound- and movable-fluid characteristics (Figures 9 and 10; Tables 1 and 2).

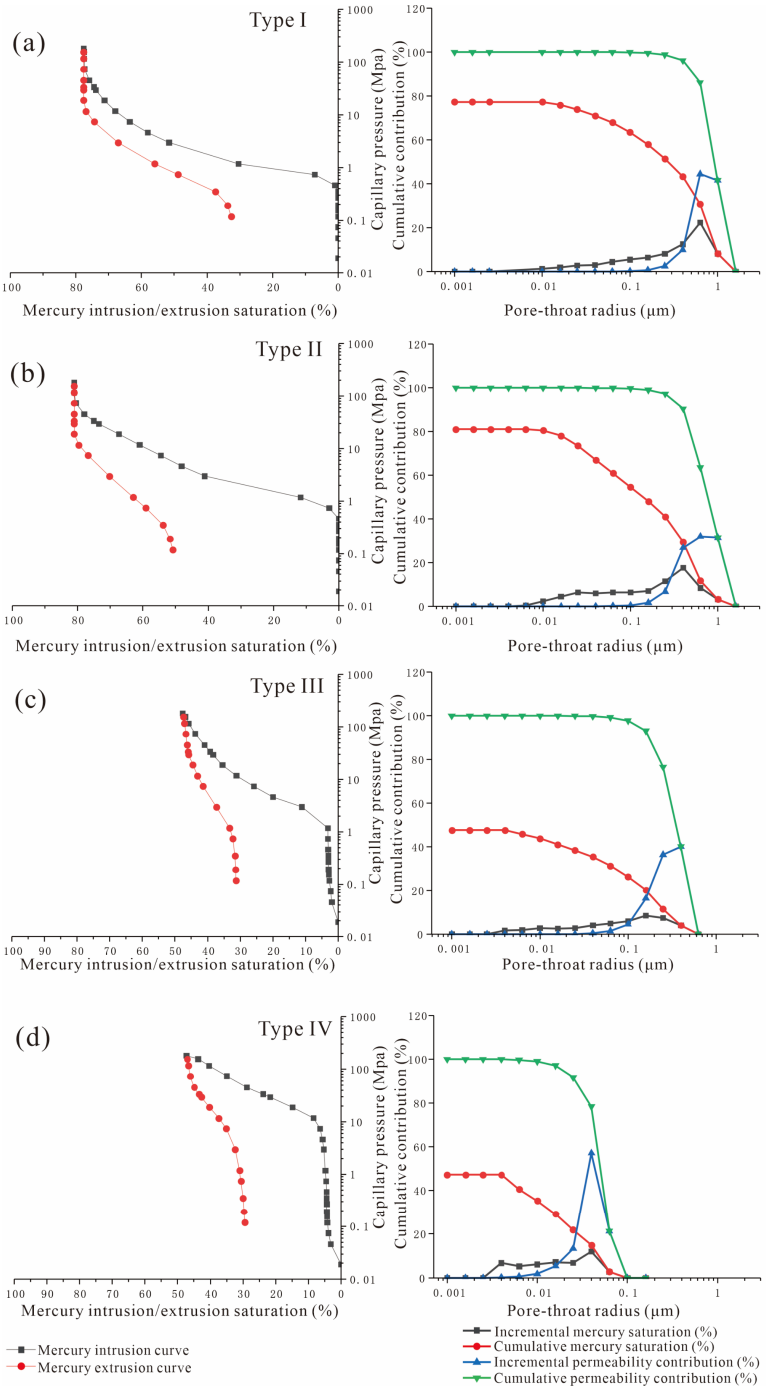


Figure 9. Representative mercury intrusion capillary pressure characteristics of the four pore-structure types in the Yageliemu Formation. (**a**) Type I; (**b**) Type II; (**c**) Type III; and (**d**) Type IV. For each pore-structure type, the left panel shows the mercury intrusion and extrusion curves, whereas the right panel shows the pore-throat-radius distributions of mercury saturation and permeability contribution.

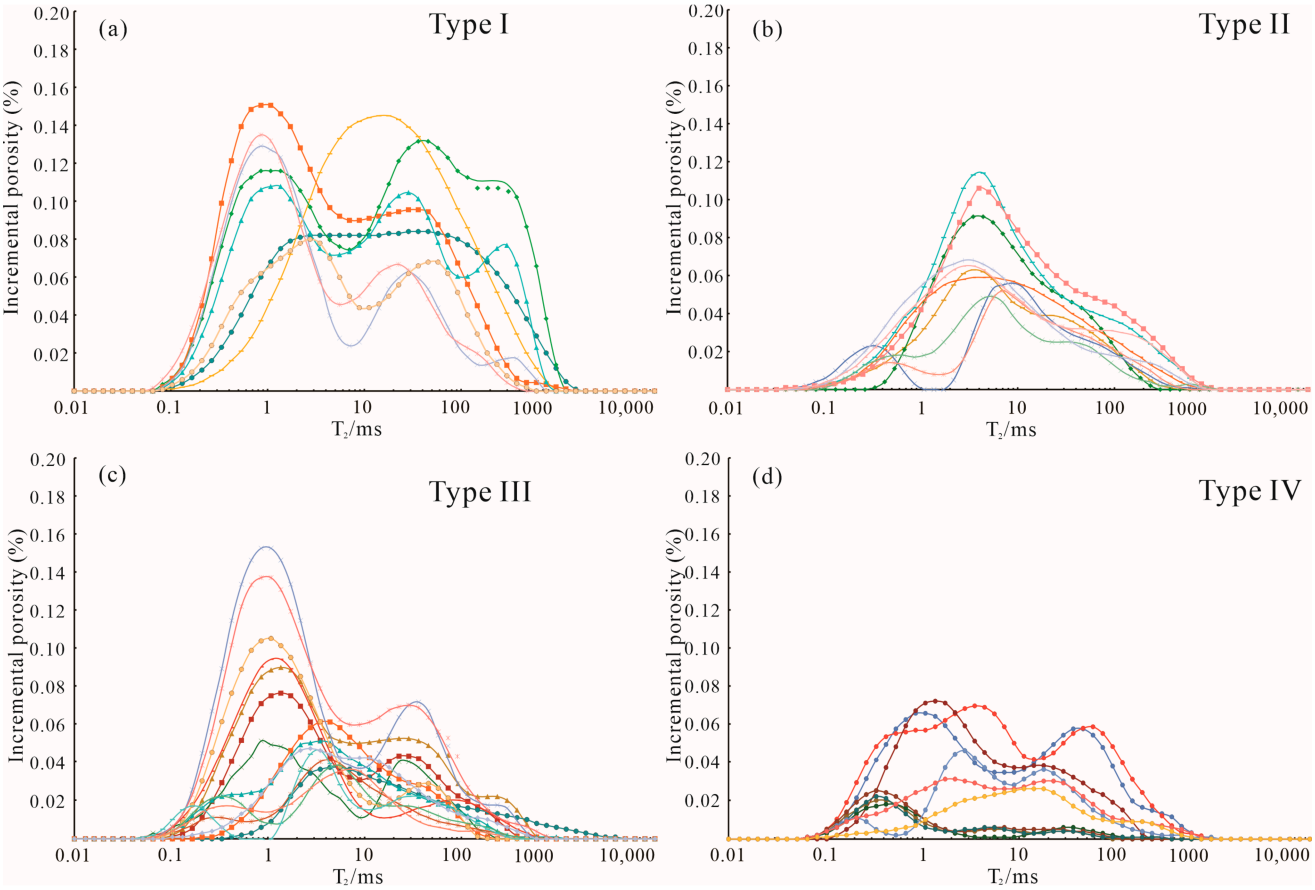


Figure 10. Water-saturated NMR T_2 distributions of the four pore-structure types in the Yageliemu Formation. (**a**) Type I; (**b**) Type II; (**c**) Type III; and (**d**) Type IV. Each curve represents an individual sample. Different colored curves represent individual samples within each pore-structure type.

Table 1. Summary of MICP parameters for the four pore-structure types in the Yageliemu Formation. Values are means, with minimum–maximum ranges in parentheses; sample numbers are indicated by n.

Type	Porosity (%)	Permeability (mD)	P_d (MPa)	P_{50} (MPa)	r_{50} (μm)	Mean Radius (μm)	Withdrawal Efficiency (%)
I (n = 16)	4.12 (2.09–6.16)	6.34 (0.01–34.07)	0.89 (0.26–1.45)	5.09 (2.83–13.55)	0.17 (0.05–0.26)	0.43 (0.09–1.95)	38.96 (27.33–50.92)
II (n = 23)	4.33 (2.94–6.98)	0.12 (0.01–0.31)	1.14 (0.47–2.74)	7.80 (2.82–17.32)	0.11 (0.04–0.26)	0.25 (0.10–0.54)	37.25 (12.58–57.98)
III (n = 10)	3.31 (1.92–5.48)	0.06 (0.02–0.21)	1.55 (0.47–4.13)	33.99 (11.33–84.01)	0.03 (0.01–0.06)	0.20 (0.06–0.41)	42.09 (33.38–50.57)
IV (n = 7)	1.89 (1.23–2.80)	0.01 (0.01–0.02)	11.02 (8.25–13.77)	95.72 (44.15–165.42)	0.01 (0.00–0.02)	0.02 (0.02–0.03)	36.57 (31.13–39.97)

Table 2. Summary of NMR parameters for the four pore-structure types in the Yageliemu Formation. Values are means, with minimum–maximum ranges in parentheses; sample numbers are indicated by n.

Type	T_2 Cutoff (ms)	Bound-Fluid Saturation (%)	Bound-Fluid Porosity (%)	Movable-Fluid Porosity (%)	Movable-Fluid Saturation (%)
I (n = 8)	29.96 (4.16–52.16)	55.55 (28.03–70.14)	1.63 (1.20–2.07)	2.00 (0.46–6.50)	44.45 (29.86–71.97)

Table 2. *Cont.*

Type	T_2 Cutoff (ms)	Bound-Fluid Saturation (%)	Bound-Fluid Porosity (%)	Movable-Fluid Porosity (%)	Movable-Fluid Saturation (%)
II (n = 10)	5.38 (2.62–12.71)	41.84 (34.70–52.33)	1.32 (0.91–1.80)	1.84 (1.29–2.81)	58.16 (47.67–65.30)
III (n = 15)	18.55 (2.10–113.40)	53.05 (34.40–73.46)	1.25 (0.70–1.59)	1.11 (0.56–1.76)	46.95 (26.54–65.60)
IV (n = 14)	14.24 (0.53–82.24)	54.93 (40.39–71.83)	0.83 (0.37–1.35)	0.72 (0.35–1.64)	45.07 (28.17–59.61)

The MICP parameters vary progressively from Type I to Type IV. Type I has an average displacement pressure of 0.89 MPa and median capillary pressure of 5.09 MPa, median and mean pore-throat radii of 0.17 and 0.43 μm, respectively, and an average permeability of 6.34 mD. Type II has an average porosity of 4.33%, compared with 4.12% for Type I, whereas its average permeability is 0.12 mD; its median capillary pressure is 7.80 MPa, and its median and mean pore-throat radii are 0.11 and 0.25 μm. Type III has an average displacement pressure of 1.55 MPa, a median capillary pressure of 33.99 MPa, and median and mean pore-throat radii of 0.03 and 0.20 μm. Type IV has an average displacement pressure of 11.02 MPa, a median capillary pressure of 95.72 MPa, median and mean pore-throat radii of 0.01 and 0.02 μm, and an average permeability of 0.01 mD (Figure 9; Table 1).

The water-saturated NMR T_2 spectra also differ among the four pore-structure types. Type I samples show broad bimodal or multimodal distributions with substantial medium- to long-T_2 components, whereas Type II samples are dominated by relatively concentrated intermediate-T_2 peaks. Type III samples commonly display complex multimodal spectra with a greater contribution from short-T_2 components, and Type IV has the lowest average NMR porosity and movable-fluid porosity. The average NMR porosities of Types I–IV are 3.62%, 4.13%, 2.94%, and 1.92%, respectively, whereas their average movable-fluid porosities are 2.00%, 1.84%, 1.11%, and 0.72%. Average movable-fluid saturation is 44.45% for Type I, 58.16% for Type II, 46.95% for Type III, and 45.07% for Type IV (Figure 10; Table 2).

4.4. Petrographic, Geochemical, and Fluid-Inclusion Characteristics of Diagenetic Minerals

Petrographic observations show tightly packed detrital grains with point, line, and point–line contacts. Grain breakage, deformation of ductile grains, and local matrix filling are also present. Carbonate minerals occur as basal, pore-filling, and fracture-filling cements, whereas authigenic silica occurs as quartz overgrowths and pore-filling crystals.

Pore-filling calcite has lower Ce/Ce* values and higher Y/Ho ratios than the other carbonate occurrences shown in Figure 11. The analyzed carbonate occurrences occupy distinct fields in Ce/Ce*–Y/Ho space, although partial overlap is present among some fracture-filling calcite and Fe-bearing carbonate data.

Feldspar and lithic fragments locally display embayed, serrated, irregular, or honeycomb -like dissolution boundaries. Feldspar dissolution pores, lithic-fragment dissolution pores, and local moldic pores occur in the analyzed samples. Thin-section and SEM observations also show pore-filling authigenic quartz, quartz overgrowths, and book-like kaolinite aggregates adjacent to some dissolution pores (Figure 12a).

Fluid inclusions occur within quartz overgrowths and pore-filling authigenic quartz (Figure 12b). The measured homogenization temperatures are concentrated mainly between approximately 105 and 135 °C (Figure 12c).

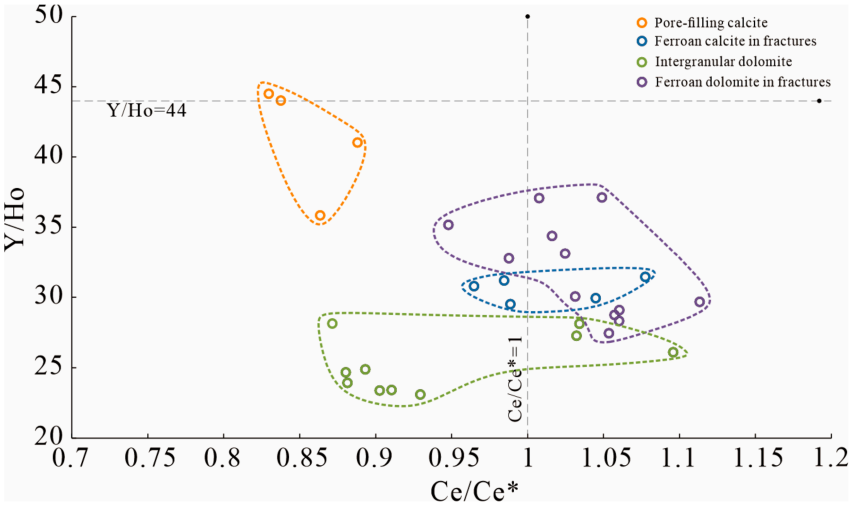


Figure 11. Ce/Ce* versus Y/Ho plot of calcites with different occurrences in the Yageliemu Formation.

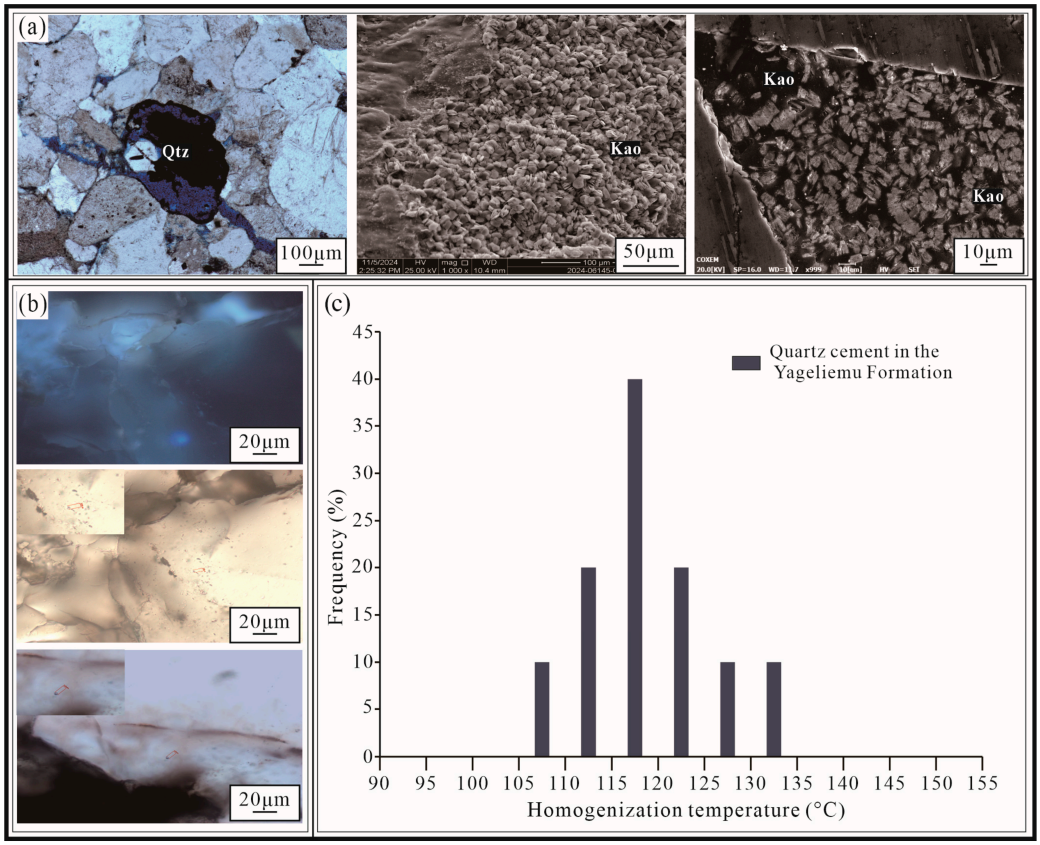


Figure 12. Petrographic characteristics of authigenic quartz and kaolinite and homogenization temperature distribution of fluid inclusions in the Yageliemu Formation. (**a**) Thin-section and SEM images showing pore-filling authigenic quartz, quartz overgrowths, and book-like kaolinite aggregates; (**b**) representative fluid inclusions hosted in quartz overgrowths and pore-filling authigenic quartz; (**c**) distribution of fluid-inclusion homogenization temperatures.

Cathodoluminescence images show relatively strong luminescence in some pore-filling calcites and weak to dark luminescence in fracture-filling calcites (Figure 13a). The different calcite occurrences also exhibit distinct major-element compositions and FeO–MnO distributions (Figure 13b,c).

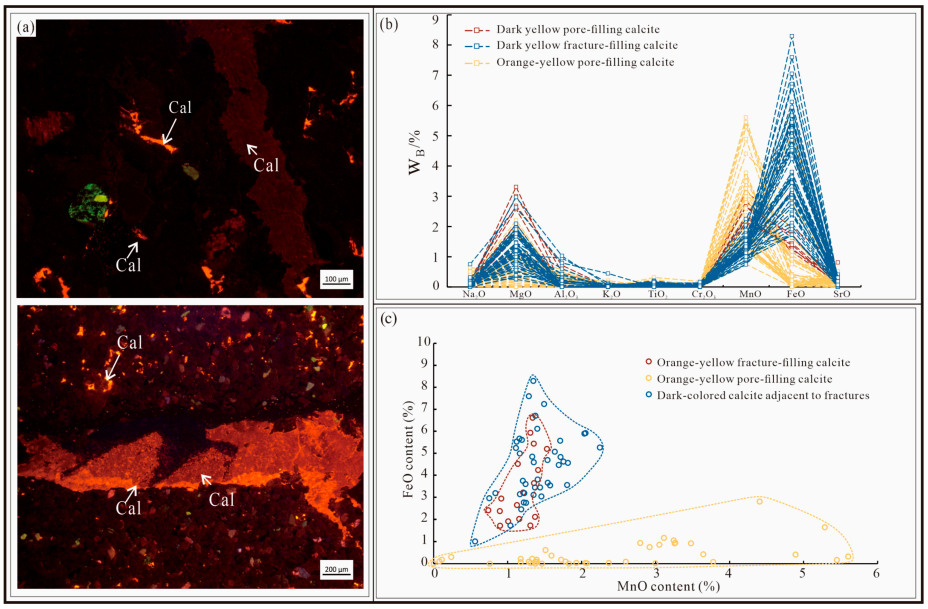


Figure 13. Cathodoluminescence and geochemical characteristics of calcites with different occurrences in the Yageliemu Formation. (**a**) Representative cathodoluminescence images of calcites with different occurrences; (**b**) major-element compositional characteristics of the calcite occurrences; (**c**) FeO–MnO distributions of the calcite occurrences.

Fe-bearing dolomite occurs as both pore-filling aggregates and fracture-filling crystals (Figure 14a). The pore-filling and fracture-filling occurrences display distinguishable chondrite-normalized rare-earth-element patterns (Figure 14b) and distributions in Ce/Ce*–U/Th space (Figure 14c).

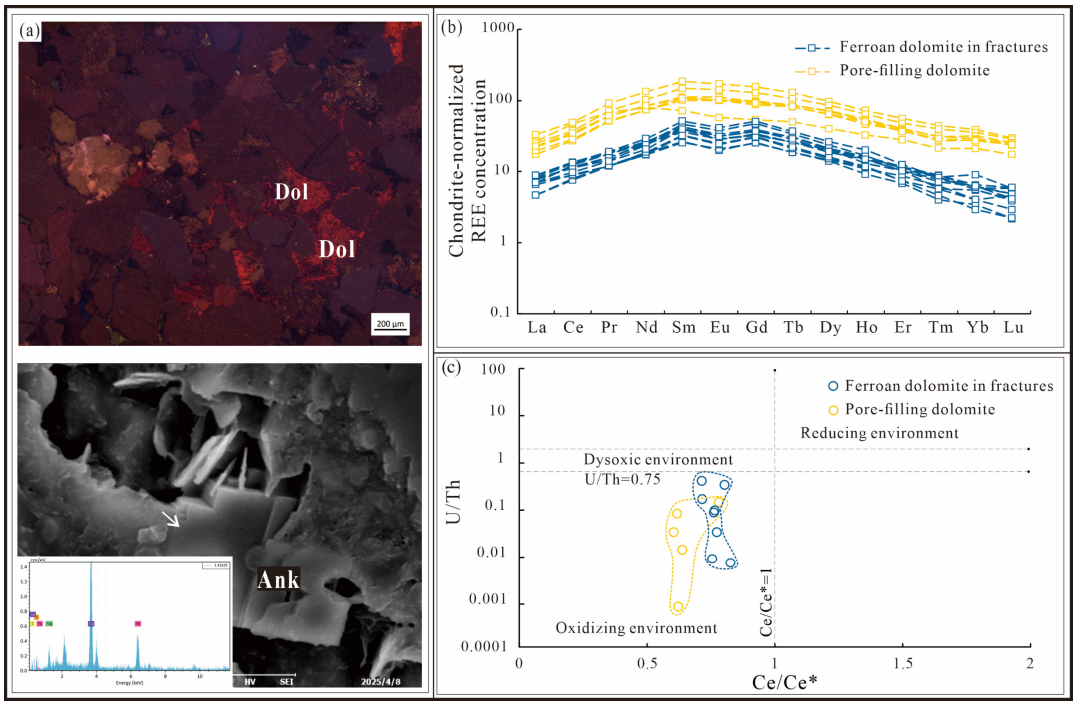


Figure 14. Cathodoluminescence and geochemical characteristics of Fe-bearing dolomites with different occurrences in the Yageliemu Formation. (**a**) Representative cathodoluminescence and SEM/EDS images of pore-filling and fracture-filling Fe-bearing dolomite; (**b**) chondrite-normalized rare-earth-element patterns of the two occurrences; (**c**) Ce/Ce*–U/Th distributions of the two occurrences.

5. Discussion

5.1. Sedimentary Preconditioning of Reservoir Heterogeneity

Sedimentary fabric established the initial spatial framework within which later reservoir modification occurred. Its influence was expressed through sand-body geometry, grain size, sorting, detrital composition, mud content, and sandstone–mudstone configuration. These properties controlled the initial arrangement of grains and pores and, more importantly, determined the susceptibility of different intervals to mechanical compaction, ductile-grain deformation, cementation, and fluid–rock interaction during burial. Comparable studies have shown that depositional facies and sedimentary texture define the initial reservoir framework, whereas the final pore system depends on the extent to which this framework is subsequently preserved or overprinted by diagenesis [10,12].

In the Ketan area, medium- to large-scale cross-bedding, erosional contacts, abrupt grain-size changes, oriented pebbles, and mud clasts record repeated channel migration and vertical stacking within a braided river delta plain succession (Figure 3). These sedimentary processes generated pronounced vertical and lateral variations in lithology and texture. The reservoirs consist predominantly of medium sandstone, pebbly sandstone, and fine conglomerate, and the investigated samples display variations in grain size, sorting, roundness, sandstone classification, and lithic-fragment composition (Figures 4–6). These variations indicate that adjacent sandstone intervals did not begin burial with identical pore frameworks or mechanical properties.

Grain size alone, however, does not adequately predict reservoir quality. Although pebbly sandstone and fine conglomerate contain relatively coarse framework grains, their potential storage advantage may be offset by poor sorting, abundant ductile lithic fragments, and locally elevated muddy matrix contents. These components promote closer grain packing, pseudomatrix formation, and early narrowing of intergranular throats during burial. In contrast, moderately sorted medium sandstone with a relatively stable grain-supported framework is more likely to retain residual intergranular pores. Therefore, the effect of sedimentary texture depends on the combined influence of grain size, sorting, framework composition, and mud content rather than on any single parameter.

The quantitative pore-structure data further demonstrate that total porosity alone does not preserve a direct record of the original sedimentary framework. Types I and II have similar average MICP porosities of 4.12% and 4.33%, respectively, but their average permeabilities are 6.34 and 0.12 mD, representing a difference of approximately 53-fold. Type I also has a lower displacement pressure and larger median and mean pore-throat radii than Type II (Figure 9; Table 1). This contrast indicates that comparable pore volumes may be organized into markedly different throat networks. Sedimentary fabric therefore influenced reservoir effectiveness by defining the initial distribution and mechanical stability of pore bodies and throats, whereas present permeability reflects the degree to which this framework was preserved, narrowed, enlarged, or reconnected during subsequent burial.

Sand-body architecture provided an additional scale of heterogeneity. Within the investigated intervals, thick and vertically stacked sandstone bodies generally provided a more continuous grain-supported framework than frequently interbedded sandstone–mudstone successions and the marginal parts of individual sand bodies. The latter commonly contain sharper textural changes, higher proportions of muddy or ductile components, and more numerous sandstone–mudstone contacts. Such intervals were more susceptible to compaction and localized cementation, whereas cleaner sandstone intervals provided more favorable initial conditions for preserving residual intergranular pores and for the later development of connected dissolution pores and fractures [10,35].

The sedimentary control identified here should therefore be regarded as a preconditioning effect rather than as the sole determinant of present reservoir quality. Depositional architecture established spatial variations in pore-framework geometry and compaction resistance, but subsequent diagenesis determined whether these initial advantages were preserved or destroyed. This distinction explains why similar lithologies or porosities may display substantially different permeability and pore-throat characteristics after deep burial. Previous work on the Cretaceous Bashijiqike Formation in the Kuqa Depression has likewise emphasized the combined influence of deep burial, pore-throat structure, diagenesis, and fractures on reservoir quality [6,36–38]. The Yageliemu Formation extends this regional model by showing that coarse-grained braided river delta deposits cannot be evaluated from grain size or porosity alone; sand-body stacking and sandstone–mudstone architecture must first be considered as the depositional template on which later diagenetic modification acts. This interpretation is also consistent with international sandstone-reservoir studies showing that depositional texture establishes initial heterogeneity, whereas compaction, cementation, dissolution, and authigenic mineral precipitation amplify or reorganize that heterogeneity during burial [10–12,39,40].

5.2. Diagenetic Modification, Pore-Space Function, and Reservoir Effectiveness

Diagenesis exerted the more direct control on the final connectivity and flow capacity of the Yageliemu Formation reservoirs. The initial differences produced by sedimentation were progressively modified by compaction, carbonate and siliceous cementation, dissolution, clay mineral transformation, and fracturing. These processes did not operate uniformly throughout the reservoir. Their effects depended on the original grain framework, sandstone–mudstone configuration, fluid accessibility, and the presence or absence of fractures. Consequently, diagenesis either preserved, weakened, or amplified the heterogeneity inherited from deposition [10,11,35].

Mechanical compaction represented the first major reduction in primary pore space. Point, line, and point–line contacts, together with grain breakage and deformation of ductile components, indicate progressive rearrangement and compression of the detrital framework. In relatively clean, rigid-grain-supported sandstones, compaction reduced pore volume but did not completely eliminate residual intergranular pores. In mud-rich or ductile-lithic-rich intervals, deformation and pseudomatrix development more readily narrowed or disconnected primary throats. Therefore, compaction established an early contrast between intervals that retained a partially connected pore framework and those that entered a strongly compacted state before later fluid modification [10,11,35].

Comparable diagenetic partitioning occurs in the deeply buried Lower Cretaceous Lower Goru sandstones of the Lower Indus Basin, where differences in compaction, quartz cementation, and authigenic clay minerals generate pronounced porosity–permeability contrasts between adjacent sandstone units [11]. More broadly, diagenesis commonly accentuates depositional heterogeneity because facies-dependent pore-water chemistry, detrital composition, and initial permeability lead to divergent burial-diagenetic pathways [10]. The Yageliemu Formation follows this general framework, but fracture-controlled fluid migration and late Fe-bearing carbonate filling impose an additional control in its ultra-deep foreland-basin setting.

Carbonate and siliceous cementation further modified this framework. Early pore-filling and basal calcite directly occupied residual intergranular pores, although local early cementation may also have increased framework rigidity and limited subsequent grain rearrangement [10,35]. The lower Ce/Ce* and higher Y/Ho values of some pore-filling calcites, together with their petrographic occurrence, are consistent with precipitation from relatively oxidizing early pore fluids (Figure 11), although these proxies should be inter-

preted collectively rather than as unique indicators of fluid conditions [41,42]. During deeper burial, authigenic quartz, kaolinite, Fe-bearing calcite, and ankerite formed in pores and fractures. Their distribution shows that cementation influenced reservoir quality not only by reducing total pore volume, but also by partitioning pore bodies and blocking the narrow throats and fractures that controlled long-range connectivity [10,35].

Dissolution was the principal pore-generating diagenetic process, but its influence on reservoir effectiveness was conditional [10,35,43,44]. Irregular and embayed dissolution boundaries in feldspar and lithic fragments, together with feldspar dissolution pores, lithic-fragment dissolution pores, and local moldic pores, document selective removal of unstable components [43,44]. Fluid inclusions in quartz overgrowths and pore-filling authigenic quartz yield homogenization temperatures mainly between approximately 105 and 135 °C, indicating that an important phase of dissolution and siliceous mineral precipitation occurred during intermediate to deep burial (Figure 12). This assemblage is interpreted to record the circulation of acidic fluids associated with burial diagenesis and hydrocarbon-related fluid activity [43,45].

Dissolution did not simply produce a uniform net increase in pore volume. Materials released during feldspar and lithic-fragment alteration may have been transported over limited distances and reprecipitated as kaolinite, authigenic quartz, quartz overgrowths, and carbonate minerals. Consequently, some dissolution pores remained isolated, whereas others were partly partitioned or refilled by authigenic precipitates. The net influence of dissolution on reservoir quality therefore depended on fluid flux, solute transport, and the location and intensity of secondary-mineral precipitation [10,35,43,44].

The principal reservoir-space components performed different functions within the effective pore system. Residual intergranular pores constituted the basic storage and connective framework because they occurred between framework grains and were more readily linked by primary or modified throats. Dissolution pores locally enlarged pore bodies and increased storage capacity, but they did not necessarily improve permeability when they remained isolated or were connected through narrow throats. Fractures generally contributed less to total pore volume than intergranular and dissolution pores, but open or weakly filled fractures could disproportionately improve permeability by connecting otherwise separated pore domains. Reservoir effectiveness therefore depended on the spatial combination of these three components rather than on the abundance of any single pore type [46,47].

The integrated MICP and NMR results quantify this distinction between pore volume, fluid occurrence, and flow capacity. From Type I to Type IV, average displacement pressure increases from 0.89 to 11.02 MPa and median capillary pressure increases from 5.09 to 95.72 MPa, whereas median throat radius decreases from 0.17 to 0.01 μm and mean pore-throat radius decreases from 0.43 to 0.02 μm (Figure 9; Table 1). Over the same sequence, average movable-fluid porosity decreases from 2.00% to 0.72% (Figure 10; Table 2). These trends record progressive restriction of the effective throat network and a reduction in the volume of fluid participating in potentially connected pore systems.

The contrast between Types I and II is particularly informative. Type II has the highest average movable-fluid saturation of 58.16%, exceeding the 44.45% average of Type I, but its permeability is substantially lower. This divergence shows that the proportion of movable fluid within pore bodies is not equivalent to bulk flow capacity. A relatively high movable-fluid saturation may occur where pore bodies contain mobile fluid but remain connected through small, poorly coordinated, or tortuous throats. MICP mainly constrains throat dimensions and capillary connectivity, whereas NMR characterizes fluid occurrence and mobility within the pore system. Their combined interpretation therefore provides a more

reliable assessment of reservoir effectiveness than either total porosity or movable-fluid saturation alone.

Fractures further amplified this heterogeneity by performing a dual role. High-angle fractures and microfracture assemblages locally connected residual intergranular pores and dissolution pores (Figures 3c and 8g–i). During fluid migration, these fractures provided preferential pathways that increased fluid–rock interaction and promoted localized dissolution and mineral precipitation [45,47,48]. When fractures remained open or only weakly filled, they improved pore-system connectivity and could account for relatively high permeability despite low matrix porosity [47,48]. During later burial, however, fractures also became preferential sites for Fe-bearing calcite and ankerite precipitation. Strong mineral filling reduced or eliminated their hydraulic effectiveness and locally isolated adjacent pore domains. Fault-related fracturing therefore enhanced reservoir quality only where later cementation remained limited [4,7–9,45,47–49].

Taken together, the results indicate a hierarchical relationship between sedimentary and diagenetic controls. Sedimentary architecture established the initial spatial distribution of grain frameworks and compaction susceptibility, whereas diagenesis more directly determined the final throat dimensions, pore connectivity, movable-fluid volume, and fracture effectiveness. The most favorable investigated intervals are therefore those in which three conditions overlap: residual intergranular pores are preserved within relatively clean and grain-supported sandstone, dissolution pores remain connected to an effective throat network, and fractures are open or only weakly filled by late carbonate cements. Conversely, high total porosity alone does not define a favorable reservoir where pore bodies are connected by narrow throats or where fractures and adjacent pores have been strongly cemented.

The Yageliemu case therefore shows that reservoir quality is not controlled by a single diagenetic reaction, but by the sequence and spatial superposition of pore destruction, pore generation, and fracture modification. Compaction and early cementation impose an initial reduction in primary pore space [10,35]; later dissolution improves storage only where secondary pores remain connected and dissolved components are not extensively reprecipitated [35,43,44]; and fracturing enhances flow only where subsequent mineral filling is limited [45,47,48]. This process-based interpretation explains why intervals with similar lithology or total porosity can evolve toward markedly different hydraulic states after deep burial.

5.3. Regional Significance and Broader Implications for Deep-Reservoir Evaluation

At the regional scale, these results refine the reservoir-quality model for the Cretaceous succession of the Kuqa Depression. Studies of the Bashijiqike Formation have documented the importance of pore-throat structure, diagenetic preservation, dissolution, and fracture modification in deep to ultra-deep tight sandstones [6,36–38]. The Yageliemu Formation shares these burial-related controls, but its braided river delta plain succession contains pronounced coarse-grained facies changes, stacked sand bodies, and sandstone–mudstone configurations. Consequently, reservoir-quality criteria developed for the Bashijiqike Formation should not be transferred to the Yageliemu Formation on the basis of lithology or porosity alone. Depositional architecture, throat-scale connectivity, and the degree of fracture filling need to be evaluated together.

The same conclusion has broader relevance to tight sandstone reservoirs outside the Kuqa Depression. In the Lower Goru Formation of the Indus Basin, depositional heterogeneity is likewise overprinted by variable compaction, quartz cementation, and authigenic clay development, producing large reservoir-quality contrasts between adjacent sandstone intervals [11,12]. More generally, sandstone diagenesis studies show that facies-

dependent initial properties can diverge strongly during burial because fluid access, cement precipitation, and dissolution vary spatially [10]. The Yageliemu Formation adds a further foreland-basin component to this framework: fractures can initially enhance connectivity and fluid transfer, but the same fractures can later become sites of Fe-bearing carbonate precipitation and lose hydraulic effectiveness. Thus, fracture abundance alone is not a reliable indicator of reservoir quality [45,47,48].

These relationships suggest a practical hierarchical workflow for reservoir evaluation. First, sedimentary architecture should be used to identify thick, relatively clean, vertically stacked sand bodies with mechanically favorable grain frameworks. Second, MICP and NMR parameters should be used jointly to determine whether pore volume is supported by an effective throat network and a measurable movable-fluid component. Third, fracture occurrence should be evaluated together with fracture-filling intensity rather than simply recorded as fracture density. Within the investigated interval, the most favorable combination is therefore preservation of residual intergranular pores, connected dissolution pores, relatively large effective throats, and open or weakly mineralized fractures. This hierarchy provides a process-based screening scheme that is more robust than ranking intervals by porosity alone.

The present dataset is primarily core-based and characterizes reservoir heterogeneity at the sampled-well and plug scales. Accordingly, extrapolation of the proposed framework between wells should be calibrated with continuous logging and, where available, seismic-scale architectural information. Nevertheless, the coupled sedimentary–diagenetic framework provides a testable basis for comparing deep tight sandstone reservoirs in other structurally active foreland-basin settings. The burial, fluid, and diagenetic evolution inferred for the Yageliemu Formation is summarized in Figure 15.

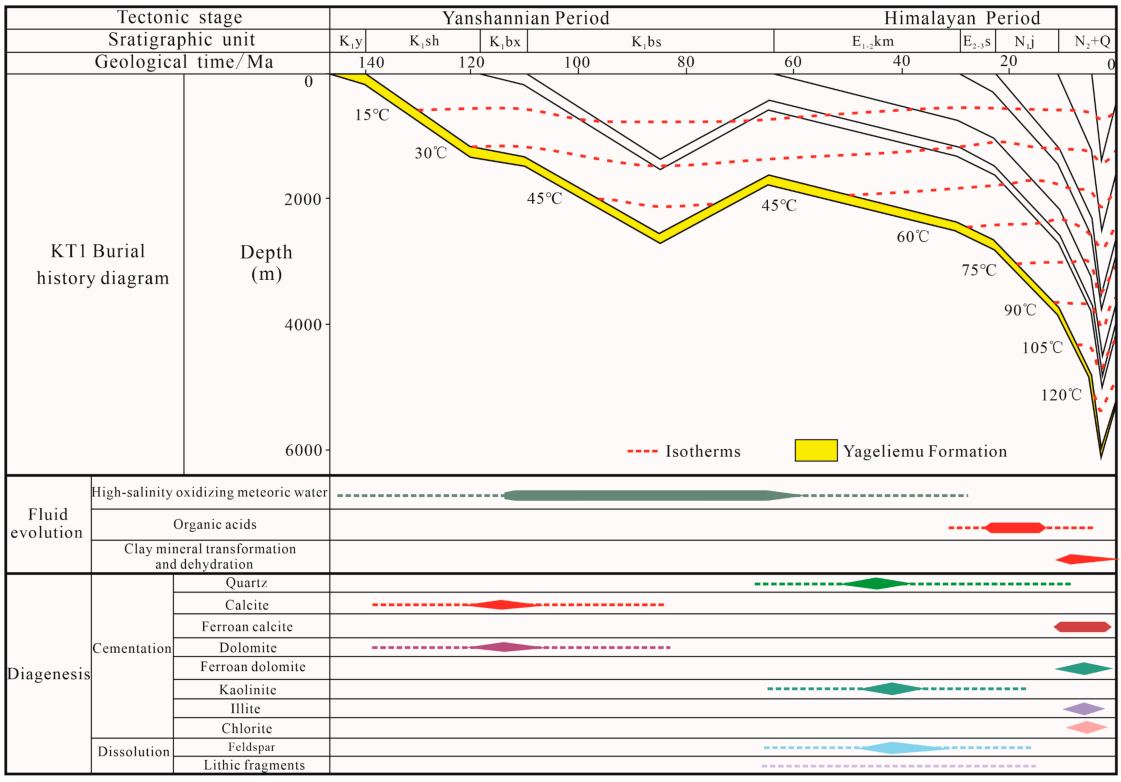


Figure 15. Burial history, fluid evolution, and diagenetic evolution model of the Yageliemu Formation. The yellow-filled interval in the burial-history diagram represents the Yageliemu Formation in Well KT1. In addition to the yellow Yageliemu Formation interval and red dashed isotherms, the colored horizontal lines and diamond-shaped symbols indicate the relative timing and duration of the corresponding fluid-evolution and diagenetic events listed on the left.

6. Conclusions

(1) Sedimentary architecture and diagenesis exerted different but complementary controls on reservoir heterogeneity. Grain size, sorting, framework composition, mud content, and sand-body stacking established the initial spatial differences in pore-framework geometry and compaction resistance. Subsequent compaction, cementation, dissolution, and fracture-related mineralization more directly determined whether this initial framework was preserved, disconnected, or locally reconstructed. Thus, sedimentation preconditioned reservoir heterogeneity, whereas diagenesis exerted the dominant control on the final pore-throat connectivity.

(2) Integrated MICP and NMR analyses demonstrate that total porosity is not an adequate predictor of reservoir effectiveness. Types I and II have similar average porosities of 4.12% and 4.33%, respectively, but their average permeabilities differ by approximately 53-fold. From Type I to Type IV, displacement and median capillary pressures increase, whereas effective throat radii, permeability, and movable-fluid porosity decrease. These results show that effective throat dimensions and connectivity, rather than pore volume alone, govern the flow capacity of the deeply buried Yageliemu reservoirs.

(3) The principal reservoir-space components perform distinct functions. Residual intergranular pores form the basic storage and connective framework; dissolution pores locally increase pore volume but improve permeability only where they remain connected to effective throats; and fractures contribute disproportionately to connectivity despite their limited volumetric contribution. Fractures therefore have a dual effect: open or weakly filled fractures improve fluid flow, whereas late Fe-bearing carbonate filling can substantially reduce their hydraulic effectiveness.

(4) Favorable reservoirs develop where sedimentary and diagenetic conditions overlap positively. The most effective intervals are characterized by a relatively stable grain-supported framework, preservation of residual intergranular pores, dissolution pores connected to the pre-existing throat network, and open or weakly mineralized fractures. Thick, relatively clean stacked sand bodies provide favorable initial conditions, but they form effective reservoirs only where strong compaction and late carbonate recementation have not destroyed the connected pore-fracture system.

Author Contributions: Conceptualization, L.Z. and J.W.; methodology, L.Z., Z.Z. and J.W.; investigation, L.Z., X.S., M.T., H.L., J.F. and H.Q.; formal analysis, L.Z. and Z.Z.; resources, H.L. and J.W.; data curation, L.Z.; writing-original draft preparation, L.Z.; writing-review and editing, J.W. and Z.Z.; visualization, L.Z. and X.S.; supervision, J.W.; project administration, H.L. and J.W.; funding acquisition, H.L. and J.W. All authors have read and agreed to the published version of the manuscript.

Funding: This research was funded by the National Science and Technology Major Project for New-Type Oil and Gas Exploration and Development (grant number 2025ZD140050203), the National Natural Science Foundation of China (grant number 42172146), the Taishan Scholars Program of Shandong Province (grant number tsqn202312111), the Evolution of Tectonic Stress Field and Reservoir Control Mechanism in Key Stratigraphic Groups of the Kuqa Foreland Zone (grant number 671024115046), and the Special Project of Fundamental Science Center at China University of Petroleum (East China) (grant number 26CX05003A).

Institutional Review Board Statement: Not applicable.

Informed Consent Statement: Not applicable.

Data Availability Statement: The data presented in this study are available on reasonable request from the corresponding author.

Acknowledgments: The authors thank the relevant laboratories and technical staff for assistance with sample preparation, petrophysical measurements, and microscopic analyses.

Conflicts of Interest: Authors Lu Zhou, Xinyu Sun, Minggang Tang, Hong Lou, Jinfeng Feng and Haihua Qiu were employed by the company Tarim Oilfield Company, PetroChina. The authors declare no conflicts of interest. The funders had no role in the design of the study; in the collection, analyses, or interpretation of data; in the writing of the manuscript; or in the decision to publish the results.

References

1. Wang, Q.; Zhu, Y.F.; Tang, Y.G.; Yang, G.; Sun, C.H.; Chen, C. Oil and gas geological conditions and exploration potential in ultra-deep formations below ten thousand meters in Tarim Basin. *Deep Earth Energy Sci. Technol.* **2025**, *1*, 36–48.
2. Zhang, R.; Yang, H.; Wang, J.; Shou, J.; Zeng, Q.; Liu, Q. Formation mechanism and petroleum exploration significance of ultra-deep low-porosity tight sandstone reservoirs in the Kuqa Depression. *Acta Pet. Sin.* **2014**, *35*, 1057–1069.
3. Wang, Q.H.; Yang, H.J.; Xu, Z.P.; Yang, X.Z.; Li, Y.; Cai, Z.Y.; Zhou, L. Major breakthrough and exploration significance of Well KT1 in the Kuqa Depression, Tarim Basin. *China Pet. Explor.* **2023**, *28*, 1–10.
4. Wang, J.P.; Zhang, H.L.; Zhang, R.H.; Yang, X.J.; Zeng, Q.L.; Chen, X.G.; Zhao, J.Q. Modification of ultra-deep tight sandstone reservoirs by fractures: A case study of the Keshen gas field, Kuqa Depression, Tarim Basin. *Oil Gas Geol.* **2018**, *39*, 77–88.
5. Gao, Z.Y.; Wang, X.Q.; Li, J.M.; Cui, J.; Jin, X.; Zhou, C.; Feng, J.; Shi, Y. Quantitative characterization and distribution of pore assemblage types in Cretaceous reservoirs of the Kelasu structural belt, Kuqa Depression. *Acta Pet. Sin.* **2018**, *39*, 645–659.
6. Lai, J.; Xiao, L.; Zhao, X.; Zhao, F.; Li, Y.; Zhu, S.; Wang, G.; Liu, H. Genesis and logging evaluation of deep to ultra-deep high-quality clastic reservoirs: A case study of the Cretaceous Bashijiqike Formation in the Kuqa Depression. *Acta Pet. Sin.* **2023**, *44*, 612–625.
7. Xu, K.; Zhang, H.; Liu, X.Y.; Wang, Z.; Lai, S. Present-day in-situ stress characteristics of deep fractured reservoirs in the Kuqa Depression and their implications for natural gas exploration and development. *Pet. Geol. Recovery Effic.* **2022**, *29*, 34–45.
8. Liu, C.; Zhang, R.; Zhang, H.; Huang, W.; Mo, T.; Zhou, L. Genetic types and geological significance of micropores in tight sandstone reservoirs: A case study of ultra-deep reservoirs in the Kuqa foreland thrust belt. *Acta Pet. Sin.* **2017**, *38*, 150–159.
9. Zhang, R.H.; Zeng, Q.L.; Li, J.; She, M.; Yu, C. Physical simulation of multistage dissolution in Cretaceous reservoirs of the Kelasu structural belt, Kuqa Depression. *Xinjiang Pet. Geol.* **2019**, *40*, 210–222.
10. Morad, S.; Al-Ramadan, K.; Ketzer, J.M.; De Ros, L.F. The impact of diagenesis on the heterogeneity of sandstone reservoirs: A review of the role of depositional facies and sequence stratigraphy. *AAPG Bull.* **2010**, *94*, 1267–1309. [CrossRef]
11. Baig, M.O.; Harris, N.B.; Ahmed, H.; Baig, M.O.A. Controls on reservoir diagenesis in the Lower Goru Sandstone Formation, Lower Indus Basin, Pakistan. *J. Pet. Geol.* **2016**, *39*, 29–47. [CrossRef]
12. Khan, M.A.; Khan, T.; Ali, A.; Bello, A.M.; Radwan, A.E. Role of depositional and diagenetic controls on reservoir quality of complex heterogenous tidal sandstone reservoirs: An example from the Lower Goru Formation, Middle Indus Basin, Southwest Pakistan. *Mar. Pet. Geol.* **2023**, *154*, 106337. [CrossRef]
13. Chen, G.; Chen, C.C.; Yan, X.F.; Chen, C.; Zhao, J. Sedimentological study of the Cretaceous Bashijiqike Formation in the Kuqa Depression based on image logs. *Adv. Geosci.* **2024**, *14*, 587–603.
14. Hu, T.; Zhang, B.Q.; Shu, Z.G. Architectural characteristics of a Cretaceous fan-delta parasequence in the Kuqa Depression. *J. Mineral. Petrol.* **2003**, *23*, 87–89.
15. Wang, T.F.; Jin, Z.K.; Li, H.; Liu, D.Q.; Cheng, R.H.; Shi, S.T.; Wang, J.Y. Processes and causes of Phanerozoic tectonic evolution of the western Tarim Basin, northwest China. *Pet. Sci.* **2020**, *17*, 623–638. [CrossRef]
16. Cui, Q.; Huangfu, P.; Li, Z.H.; Zhao, J.; Pei, X.; Shi, Y. Tarim rotation mechanism and the differential deformation responses along the Tian Shan. *Geophys. J. Int.* **2024**, *238*, 1023–1042. [CrossRef]
17. Izquierdo-Llavall, E.; Roca, E.; Xie, H.; Pla, O.; Muñoz, J.A.; Rowan, M.G.; Yuan, N.; Huang, S. Influence of overlapping décollements, syntectonic sedimentation, and structural inheritance in the evolution of a contractional system: The Central Kuqa fold-and-thrust belt (Tian Shan Mountains, NW China). *Tectonics* **2018**, *37*, 2608–2632. [CrossRef]
18. Wen, L.; Yang, H.J.; Li, Y.J.; Peng, G.; Yang, X.; Huang, Z.; Luo, J.; Zhang, Q. Late Cenozoic fold-and-thrust belt in the Kuqa area, southern Tianshan. *Acta Petrol. Sin.* **2016**, *32*, 847–855.
19. Chen, S.; Tang, L.; Jin, Z.; Jia, C.; Pi, X. Thrust and fold tectonics and the role of evaporites in deformation in the Western Kuqa Foreland of Tarim Basin, Northwest China. *Mar. Pet. Geol.* **2004**, *21*, 1027–1042. [CrossRef]
20. Li, C.; Yin, H.; Wu, Z.; Zhou, P.; Wang, W.; Ren, R.; Guan, S.; Li, X.; Luo, H.; Jia, D. Effects of salt thickness on the structural deformation of foreland fold-and-thrust belt in the Kuqa Depression, Tarim Basin: Insights from discrete element models. *Front. Earth Sci.* **2021**, *9*, 655173. [CrossRef]

21. Jiang, T.; Xiao, X.; Sun, X. Development strategy and theoretical and technological innovations in Kelasu ultra-deep clastic gas field. *Deep Earth Energy Sci. Technol.* **2025**, *1*, 86–94.
22. Jia, C.; Zhou, X.; Wang, Z.; Li, Q.; Pi, X.; Cai, Z.; Hu, X. Petroleum geological characteristics of Kela-2 gas field. *Chin. Sci. Bull.* **2002**, *47*, 94–99. [CrossRef]
23. Zhang, L.; Lou, H.; Wang, X.; Jiang, L.; Li, L. Characteristics of whole petroleum system and hydrocarbon accumulation mode in the Jurassic coal measures in Kuqa Depression, Tarim Basin. *Deep Earth Energy Sci. Technol.* **2025**, *1*, 1–14.
24. Zeng, L.; Wang, H.; Gong, L.; Liu, B. Impacts of the tectonic stress field on natural gas migration and accumulation: A case study of the Kuqa Depression in the Tarim Basin, China. *Mar. Pet. Geol.* **2010**, *27*, 1616–1627. [CrossRef]
25. *SY/T 5368-2016*; Identification for Thin Section of Rocks. National Energy Administration: Beijing, China, 2016.
26. Pszonka, J.; Wendorff, M. Cathodoluminescence-revealed diagenesis of carbonates and feldspars in Cergowa sandstones (Oligocene), Outer Carpathians. *Gospod. Surowcami Miner.—Miner. Resour. Manag.* **2014**, *30*, 21–36. [CrossRef]
27. Pszonka, J.; Wendorff, M. Carbonate cements and grains in submarine fan sandstones—The Cergowa Beds (Oligocene, Carpathians of Poland) recorded by cathodoluminescence. *Int. J. Earth Sci.* **2017**, *106*, 269–282. [CrossRef]
28. *GB/T 29172-2012*; Practices for Core Analysis. Standardization Administration of China: Beijing, China, 2012.
29. *GB/T 29171-2023*; Rock Capillary Pressure Measurement. Standardization Administration of China: Beijing, China, 2023.
30. Washburn, E.W. Note on a Method of Determining the Distribution of Pore Sizes in a Porous Material. *Proc. Natl. Acad. Sci. USA* **1921**, *7*, 115–116. [CrossRef] [PubMed]
31. *SY/T 6490-2023*; Specification for Measurement of Rock NMR Parameter in Laboratory. National Energy Administration: Beijing, China, 2023.
32. Gao, H.; Li, H. Determination of movable fluid percentage and movable fluid porosity in ultra-low permeability sandstone using nuclear magnetic resonance (NMR) technique. *J. Pet. Sci. Eng.* **2015**, *133*, 258–267. [CrossRef]
33. *EJ/T 1105-1999*; Determination of Temperature of Fluid Inclusions in Minerals. China Nuclear Industry Corporation: Beijing, China, 1999.
34. Goldstein, R.H. Fluid inclusions in sedimentary and diagenetic systems. *Lithos* **2001**, *55*, 159–193. [CrossRef]
35. Lee, E.Y.; Fathy, D.; Xiang, X.; Spahić, D.; Ahmed, M.S.; Fathi, E.; Sami, M. Middle Miocene syn-rift sequence on the central Gulf of Suez, Egypt: Depositional environment, diagenesis, and their roles in reservoir quality. *Mar. Pet. Geol.* **2025**, *174*, 107305. [CrossRef]
36. Lai, J.; Li, D.; Bai, T.; Zhao, F.; Ai, Y.; Liu, H.; Cai, D.; Wang, G.; Chen, K.; Xie, Y. Reservoir quality evaluation and prediction in ultra-deep tight sandstones in the Kuqa Depression, China. *J. Struct. Geol.* **2023**, *170*, 104850. [CrossRef]
37. Jia, J.H.; Gu, J.Y. Control factors and porosity evolution of high-quality sandstone reservoirs of Kela-2 gas field in Kuqa Depression. *Chin. Sci. Bull.* **2002**, *47*, 100–106. [CrossRef]
38. Zeng, Q.; Mo, T.; Zhao, J.; Tang, Y.; Zhang, R.; Xia, J.; Hu, C.; Shi, L. Characteristics, genetic mechanism and oil & gas exploration significance of high-quality sandstone reservoirs deeper than 7000 m: A case study of the Bashijiqike Formation of Lower Cretaceous in the Kuqa Depression, NW China. *Nat. Gas Ind. B* **2020**, *7*, 317–327. [CrossRef]
39. Chen, J.; Yao, J.; Mao, Z.; Li, Q.; Luo, A.; Deng, X.; Shao, X. Sedimentary and diagenetic controls on reservoir quality of low-porosity and low-permeability sandstone reservoirs in Chang 10, Upper Triassic Yanchang Formation in the Shanbei area, Ordos Basin, China. *Mar. Pet. Geol.* **2019**, *105*, 204–221. [CrossRef]
40. Zhang, Q.; Wu, X.-S.; Radwan, A.E.; Wang, B.-H.; Wang, K.; Tian, H.-Y.; Yin, S. Diagenesis of continental tight sandstone and its control on reservoir quality: A case study of the Quan 3 Member of the Cretaceous Quantou Formation, Fuxin uplift, Songliao Basin. *Mar. Pet. Geol.* **2022**, *145*, 105883. [CrossRef]
41. Alibo, D.S.; Nozaki, Y. Rare earth elements in seawater: Particle association, shale-normalization, and Ce oxidation. *Geochim. Cosmochim. Acta* **1999**, *63*, 363–372. [CrossRef]
42. Cao, C.; Liu, X.-M.; Bataille, C.P.; Liu, C. What do Ce anomalies in marine carbonates really mean? A perspective from leaching experiments. *Chem. Geol.* **2020**, *532*, 119413. [CrossRef]
43. Yuan, G.; Cao, Y.; Jia, Z.; Gluyas, J.; Yang, T.; Wang, Y.; Xi, K. Selective dissolution of feldspars in the presence of carbonates: The way to generate secondary pores in buried sandstones by organic CO2. *Mar. Pet. Geol.* **2015**, *60*, 105–119. [CrossRef]
44. Yuan, G.; Cao, Y.; Gluyas, J.; Jia, Z. Reactive transport modeling of coupled feldspar dissolution and secondary mineral precipitation and its implication for diagenetic interaction in sandstones. *Geochim. Cosmochim. Acta* **2017**, *207*, 232–255. [CrossRef]
45. Liu, C.; Rong, H.; Chen, S.; Jia, J.; Tang, Y.; Deng, Y. Occurrence, mineralogy and geochemistry of fracture fillings in tight sandstone and their constraints on multiple-stage diagenetic fluids and reservoir quality: An example from the Kuqa foreland thrust belt, Tarim Basin, China. *J. Pet. Sci. Eng.* **2021**, *201*, 108409. [CrossRef]
46. Lai, J.; Wang, G.; Wang, Z.; Chen, J.; Pang, X.; Wang, S.; Zhou, Z.; He, Z.; Qin, Z.; Fan, X. A review on pore structure characterization in tight sandstones. *Earth-Sci. Rev.* **2018**, *177*, 436–457. [CrossRef]
47. Liu, G.; Zeng, L.; Zhu, R.; Gong, L.; Ostadhassan, M.; Mao, Z. Effective fractures and their contribution to the reservoirs in deep tight sandstones in the Kuqa Depression, Tarim Basin, China. *Mar. Pet. Geol.* **2021**, *124*, 104824. [CrossRef]

48. Wang, J.; Wang, H.; Zhang, R.; Dong, L.; Wang, K.; Zhang, Z. Improvement of reservoir quality of ultra-deep tight sandstones by tectonism and fluid: A case study of Keshen gas field in Tarim Basin, western China. *Petroleum* **2023**, *9*, 124–134. [CrossRef]
49. Liu, X.; Ma, X.; Neng, Y.; Zhao, Y.; Ni, C.; Li, Q.; Qu, Y. Tectonic physical simulation based fracture distribution characteristics in fault anticlines in Kelasu Structural Belt: A case study of Keshen 5 and Keshen 24 structures. *Deep Earth Energy Sci. Technol.* **2025**, *1*, 25–34.

Disclaimer/Publisher's Note: The statements, opinions and data contained in all publications are solely those of the individual author(s) and contributor(s) and not of MDPI and/or the editor(s). MDPI and/or the editor(s) disclaim responsibility for any injury to people or property resulting from any ideas, methods, instructions or products referred to in the content.